Research Square

Preprints are preliminary reports that have not undergone peer review.
They should not be considered conclusive, used to inform clinical practice,
or referenced by the media as validated information.

Mössbauer study of RFeO3 (R = Y, Tb, Dy, Ho, and Er)

Hyun Ho An
Konyang University
Sung Baek Kim
physics@konyang.ac.kr

Konyang University

Research Article

Keywords: Rare-earth orthoferrites, Perovskite, Mössbauer spectroscopy, Raman spectroscopy

Posted Date: November 16th, 2026

DOI: https://doi.org/10.21203/rs.3.rs-11616362/v1

License: This work is licensed under a Creative Commons Attribution 4.0 International License.
Read Full License

Additional Declarations: No competing interests reported.

Mössbauer study of $RFeO_3$ (R = Y, Tb, Dy, Ho, and Er)

Hyun Ho An, Sung Baek Kim*

Department of Biomedical Materials, Konyang University, Daejeon 35365, Korea

Abstract

$RFeO_3$ (R = Y, Tb, Dy, Ho, and Er) powders were synthesized by sol–gel auto-combustion. Diffraction and Raman measurements revealed composition-dependent structural and vibrational changes. Magnetic rare-earth compositions exhibited larger magnetization at 20 kOe but lower coercivity and remanence than $YFeO_3$. All room-temperature Mössbauer spectra showed a single magnetic sextet, with isomer shifts of 0.24 mm/s and hyperfine fields of 497.2-500.9 kOe, consistent with high-spin Fe^{3+}. $YFeO_3$ displayed enhanced low-frequency permittivity accompanied by substantial loss. These results show that composition-dependent macroscopic responses coexist with broadly similar local Fe hyperfine environments.

Article Highlights

- Changing the rare-earth element alters the lattice dimensions and magnetic response.
- Local iron environments remain broadly similar across the five compositions.
- $YFeO_3$ shows enhanced low-frequency permittivity together with substantial dielectric loss.

Keywords

Rare-earth orthoferrites, Perovskite, Mössbauer spectroscopy, Raman spectroscopy

*Corresponding Author: physics@konyang.ac.kr

Introduction

Rare-earth orthoferrites, $RFeO_3$ (R = Y or a rare-earth element), are of interest because of their composition-dependent structural and magnetic properties. Orthorhombic members of this series adopt a distorted perovskite structure, commonly described using the *Pnma* (or equivalent *Pbnm*) setting[1-2]. The Fe sublattice exhibits predominantly antiferromagnetic ordering, while spin canting associated with the Dzyaloshinskii-Moriya interaction can produce a weak ferromagnetic component[3-4]. The structural and magnetic characteristics of these compounds are influenced by the R-site composition[5], providing opportunities to investigate the relationships between lattice distortion and magnetic response. Understanding these relationships requires complementary information on the average crystal structure, macroscopic magnetic properties, and local environment of Fe ions.

The influence of the R-site involves both ionic size and magnetic character. Variations in R^{3+} ionic radius modify octahedral tilting and the geometry of the Fe-O-Fe network, thereby affecting the magnetic exchange interactions[6]. In compounds containing magnetic rare-earth ions, interactions between the R and Fe sublattices provide an additional contribution to the magnetic behavior. The composition-dependent structural distortions are also reflected in the lattice dynamics[2]. Consequently, the composition dependence of magnetic properties should be considered in terms of both structural characteristics and the magnetic nature of the R-site ion, rather than ionic size alone.

Comparative studies have examined how R-site composition influences the structural, magnetic, and electrical properties of orthoferrites[5, 7-8]. For example, Nakhaei and Khoshnoud investigated sol-gel-combustion-derived $RFeO_3$ nanoparticles with R = Dy, Ho, Yb, and Lu, reporting composition-dependent magnetic hysteresis and dielectric responses within the orthorhombic series[5]. These studies provide a basis for examining how macroscopic property differences relate to the local electronic and magnetic environments of Fe ions.

^{57}Fe Mössbauer spectroscopy provides information on the local Fe environment through the isomer shift, electric quadrupole interaction, and magnetic hyperfine field[9-10]. Comparing these parameters with diffraction and magnetization results allows composition-dependent changes in the average crystal structure and bulk magnetic response to be examined alongside the local Fe characteristics.

In this context, $YFeO_3$ provides a reference containing a nonmagnetic R-site ion for comparison with $TbFeO_3$, $DyFeO_3$, $HoFeO_3$, and $ErFeO_3$, which contain magnetic rare-earth ions. This series provides a comparative framework for considering both R-site ionic size and magnetic character.

In this study, orthorhombic $RFeO_3$ (R = Y, Tb, Dy, Ho, and Er) powders were synthesized via a sol-gel auto-combustion method. In the figures and tables, YFO, TFO, DFO, HFO, and EFO denote $YFeO_3$, $TbFeO_3$, $DyFeO_3$, $HoFeO_3$, and $ErFeO_3$, respectively. The phase composition and crystal structures were examined by X-ray diffraction and Rietveld refinement. Raman spectroscopy, vibrating sample magnetometry, and dielectric measurements were used to investigate lattice vibrations, magnetic responses, and frequency-dependent electrical behavior, respectively. ^{57}Fe Mössbauer spectroscopy was employed to examine the Fe valence state and local hyperfine environments. By comparing these complementary measurements, this study examines whether composition-dependent differences in lattice structure and macroscopic magnetic response are accompanied by changes in the local Fe environment.

Experimental details

Materials

Iron(III) nitrate nonahydrate ($Fe(NO_3)_3 \cdot 9H_2O$, 98%), yttrium(III) nitrate hexahydrate ($Y(NO_3)_3 \cdot 6H_2O$, 99.8%), terbium(III) nitrate pentahydrate ($Tb(NO_3)_3 \cdot 5H_2O$), 99.9%), dysprosium(III) nitrate pentahydrate ($Dy(NO_3)_3 \cdot 5H_2O$, 99.9%), holmium(III) nitrate pentahydrate ($Ho(NO_3)_3 \cdot 5H_2O$, 99.9%), erbium(III) nitrate pentahydrate ($Er(NO_3)_3 \cdot 5H_2O$, 99.9%), and citric acid (99.7%) were purchased from Sigma-Aldrich (USA). Aqueous ammonia solution (NH_4OH, 25-30%) was purchased from Daejung Chemicals & Metals Co., Ltd. (Republic of Korea).

Synthesis of $RFeO_3$(R=Y, Tb, Dy, Ho, and Er) powder

Polycrystalline $RFeO_3$ (R = Y, Tb, Dy, Ho, and Er) powders were synthesized via a sol-gel auto-combustion method. Stoichiometric amounts of the corresponding R(III) nitrate and Fe(III) nitrate were dissolved in deionized water. Citric acid was then added as a chelating agent and fuel at a citric acid:total metal ion molar ratio of 1:1. The pH of the solution was adjusted to 7 by the dropwise addition of ammonia solution. The resulting solution was continuously stirred at 80 °C until a homogeneous gel was formed. Further heating of the gel on a hot plate induced self-combustion, yielding a voluminous, fluffy precursor powder. The precursor powder was collected, ground, and calcined at 850 °C for 5 h in air. After calcination, the powder was reground to obtain the final $RFeO_3$ powder.

Characterization

The crystal structure and phase purity of the synthesized samples were confirmed using X-ray diffraction (XRD) with a Bruker D2 Phaser diffractometer employing CuKα radiation ($\lambda = 1.5406$ Å). Data were collected over a 2θ range of 10-80° with a step size of 0.04° and a counting time of 0.4 s/step. Lattice parameters were refined using the FullProf program.

Raman spectra were recorded using a LabRAM HR-800 Raman spectrometer (HORIBA) with 532 nm laser excitation and a grating with 1800 grooves/mm. Each spectrum was acquired using an acquisition time of 10 s per accumulation and 10 accumulations. The band positions used for compositional comparison were determined by fitting the observed bands with Gaussian functions.

Magnetic properties were measured at room temperature using a Lakeshore 8600 vibrating sample magnetometer (VSM) under an applied magnetic field of ±20 kOe. Parameters such as net magnetization at ±20 kOe (M_{net}), remanent magnetization (M_r), and coercive field (H_c) were extracted from the magnetic hysteresis loop and compared across the $RFeO_3$ series.

Mössbauer spectra were recorded at 295 K (conventional transmission geometry with a ^{57}Co gamma-ray source (50 mCi) in the Rh matrix) to investigate the local magnetic environment of Fe ions. The Doppler velocity scale was calibrated by Fe metal foil at 295 K. Hyperfine field (H_{hf}), isomer shift (IS), and quadrupole splitting (QS) values were obtained for each compound to confirm the magnetic ordering and valence state of iron ions.

Dielectric properties were measured using an LCR meter (MFIA, Zurich instruments) in the frequency range of 10 Hz to 1 MHz at room temperature. Circular pellets (10 mm diameter, 1.2 mm thickness) of $RFeO_3$ powders were gold-coated to ensure good electrical contact. The dielectric constant (ε') and dielectric loss (tan δ) were recorded as functions of frequency.

Results and discussion

Structural and phase analysis

Figure 1(a) shows the X-ray diffraction patterns and Rietveld refinement profiles of $RFeO_3$ (R = Y, Tb, Dy, Ho, and Er) powders. The diffraction patterns are consistent with an orthorhombic structure (space group: *Pbnm*). No additional crystalline phases are apparent in the presented patterns. The calculated profiles reproduce the principal diffraction features, supporting the assignment of the orthorhombic structure across the series.

The enlarged diffraction patterns in Figure 1(b) reveal a systematic shift of the principal diffraction feature near $2\theta = 33°$ toward higher angles in the sequence $TbFeO_3$, $DyFeO_3$, $YFeO_3$, $HoFeO_3$, and $ErFeO_3$, corresponding to decreasing R^{3+} ionic radius. According to Bragg's law, the shift toward higher diffraction angles corresponds to a reduction in the associated interplanar spacing. This observation is consistent with contraction of the lattice as the R-site ionic radius decreases.

The structural parameters are summarized in Table 1. As the R^{3+} ionic radius decreases from 104 pm for Tb^{3+} to 100.4 pm for Er^{3+}, the lattice parameter *a* decreases from 5.3283 to 5.2629 Å, while *b* and *c* decrease from 5.5983 to 5.5811 Å and from 7.6430 to 7.5951 Å, respectively. The unit-cell volume decreases from $TbFeO_3$ (227.9863 $Å^3$) to $ErFeO_3$ (223.0891 $Å^3$). The changes in lattice dimensions differ among the crystallographic directions, with the largest absolute change occurring along the a axis. The unequal changes in the lattice parameters indicate anisotropic lattice contraction across the series. This behavior is consistent with the directional response of the tilted orthorhombic perovskite framework to variations in R-site ionic size. $YFeO_3$ falls between $DyFeO_3$ and $HoFeO_3$ in both ionic radius and unit cell volume, following the overall structural trend.

The Goldschmidt tolerance factor (t) was calculated using the following equation:

$$t = \frac{r_R + r_O}{\sqrt{2}(r_{Fe} + r_O)} \quad (1)$$

where r_R, r_{Fe}, and r_O are the ionic radii of R^{3+}, Fe^{3+}, and O^{2-}, respectively. Figure 1(c) presents the variation of the lattice parameters and unit-cell volume with tolerance factor. The tolerance factor decreases from 0.8436 for $TbFeO_3$ to 0.8312 for $ErFeO_3$, accompanied by a reduction in lattice dimensions. This trend is consistent with the influence of R-site ionic size on the distorted perovskite framework. Combined diffraction and Raman studies of $RFeO_3$ have shown that the response of octahedral tilting and lattice dynamics to pressure depends on the rare-earth cation size[11]. However, the tolerance factor is a geometric descriptor rather than a direct measurement of the FeO_6 tilt angles. These structural trends provide a basis for comparing the Raman spectra, magnetic responses, and Fe hyperfine parameters discussed in the following sections.

Raman spectroscopy analysis

Figure 2(a) shows the Raman spectra of $RFeO_3$ (R = Y, Tb, Dy, Ho, and Er) powders in the range of 100-700 cm^{-1}. The four lanthanide orthoferrites exhibit broadly similar spectral features, with prominent low-frequency bands and several weaker bands at higher frequencies. In contrast, $YFeO_3$ displays a distinct distribution of bands, particularly below approximately 300 cm^{-1}. Seven observed bands in the lanthanide orthoferrites were labeled P1-P7 for identification and comparison across the four compositions. These labels do not denote specific vibrational symmetries. The center positions of the bands, obtained by fitting with Gaussian functions, are summarized in Table 2.

Previous work combining polarized Raman spectroscopy and first-principles calculations reported that vibrations below approximately 200 cm^{-1} in orthorhombic $RFeO_3$ are generally dominated by rare-earth-ion displacements, whereas oxygen-ion displacements dominate above approximately 300 cm^{-1}, with both contributing in the intermediate region[2]. The bands P1-P3, P5-P7, and P4 in the present study lie within these respective frequency regions.

Figure 2(b) presents the fitted positions of P1-P3 as a function of the R^{3+} ionic radius. P1 and P2 exhibit small, nonmonotonic variations within 105.00-105.64 and 133.10-133.42 cm^{-1}, respectively. In contrast, P3 shifts progressively toward lower frequencies from 152.14 cm^{-1} in $ErFeO_3$ to 151.36, 150.12, and 149.35 cm^{-1} in $HoFeO_3$, $DyFeO_3$, and $TbFeO_3$, respectively. Although these bands lie in the frequency region generally dominated by rare-earth-ion displacements, this classification alone does not establish that their composition dependence is governed by the rare-earth mass. The respective contributions of mass and structural changes cannot be separated in the present analysis.

More pronounced redshifts are observed for P4-P7, as shown in Figure 2(c). With increasing R^{3+} ionic radius from Er^{3+} to Tb^{3+}, P4 shifts from 262.94 to 246.64 cm^{-1}, P5 from 326.41 to 310.53 cm^{-1}, P6 from 412.18 to 393.17 cm^{-1}, and P7 from 486.72 to 467.01 cm^{-1}. All four bands decrease monotonically through the Er-Ho-Dy-Tb sequence. These redshifts accompany the increase in lattice dimensions and unit-cell volume identified by

XRD, showing that the R-site-dependent structural evolution is also reflected in the vibrational spectra.

The shifts of P4-P7 are qualitatively consistent with changes in the octahedral framework and the associated vibrational restoring forces. Weber et al. reported an overall decrease in orthoferrite Raman frequencies with increasing rare-earth ionic radius and demonstrated that the frequencies of two specifically identified rotational modes scale with the corresponding FeO_6 tilt angles[2]. Variations in lattice dimensions, octahedral tilting, and bond geometry therefore provide a plausible structural basis for the observed frequency trends.

$YFeO_3$ is included in Figure 2(a) but excluded from the band-position plots because a reliable one-to-one correspondence between its observed features and P1-P7 has not been established. Its distinct spectral profile alone does not demonstrate a different crystal phase. Overall, the Raman results reveal small, nonmonotonic variations in P1 and P2 and systematic redshifts of P3-P7 with increasing R^{3+} ionic radius within the lanthanide series. Together with the XRD results, these observations provide complementary evidence of composition-dependent changes in lattice dimensions and vibrational characteristics.

Magnetic properties

Figure 3 shows the room-temperature magnetization-field (M-H) curves of $RFeO_3$ (R = Y, Tb, Dy, Ho, and Er) powders measured over an applied field range of -20 to +20 kOe. The lanthanide orthoferrites exhibit a predominantly field-dependent, approximately linear magnetization response with relatively narrow hysteresis, whereas $YFeO_3$ displays a substantially broader loop and a smaller magnetization at the maximum applied field. Since the curves do not show clear saturation within the measured field range, the magnetization at the maximum applied field is denoted M_{net}, rather than saturation magnetization. The corresponding M_{net}, coercive field (H_c), and remanent magnetization (M_r) values are summarized in Table 3.

$HoFeO_3$ exhibits the largest M_{net} (3.5535 emu/g), and all four orthoferrites containing magnetic rare-earth ions show larger M_{net} values than $YFeO_3$. This trend is consistent with an additional field-induced contribution from the magnetic R^{3+} ions. Belov et al. reported larger room-temperature susceptibilities for orthoferrites containing magnetic rare-earth ions than for $LaFeO_3$ with a nonmagnetic R-site ion, attributing the principal contribution to the rare-earth ions[12].

A different compositional dependence is observed for the hysteresis parameters. Despite having the smallest M_{net}, $YFeO_3$ exhibits the largest H_c (10,294 Oe) and M_r (0.4888 emu/g). In comparison, the lanthanide orthoferrites show markedly lower values, with H_c ranging from 179.63 to 406.19 Oe and M_r ranging from 0.0325 to 0.0864 emu/g. Thus, a larger high-field magnetization does not necessarily correspond to greater remanence or coercivity, indicating distinct compositional trends in these magnetic parameters.

Overall, the four orthoferrites containing magnetic rare-earth ions exhibit larger M_{net} values but lower coercivity and remanence than $YFeO_3$. This contrast indicates that the larger high-field magnetization associated with the magnetic R-site ions is not accompanied by a stronger irreversible magnetic response. Moreover, the M_{net} values do not vary monotonically with R^{3+} ionic radius, unlike the systematic lattice-volume trend observed by XRD. The magnetic response therefore cannot be explained by ionic size alone, and the

magnetic character of the R-site must also be considered. The Mössbauer analysis in the next section provides complementary information on the local Fe environment.

Mössbauer spectroscopy

Figure 4 shows the room-temperature ^{57}Fe Mössbauer spectra of $RFeO_3$ (R = Y, Tb, Dy, Ho, and Er) powders. All spectra exhibit six-line magnetic splitting and were fitted using a single Lorentzian sextet. The corresponding magnetic hyperfine field (H_{hf}), quadrupole splitting (QS), isomer shift (IS), and relative spectral area are summarized in Table 4. No additional doublet or distinct secondary sextet is resolved in the presented spectra. The magnetic splitting supports the presence of a magnetically ordered Fe state at room temperature on the Mössbauer timescale.

The fitted IS values are 0.24 mm/s for all five compositions at the reported precision, while H_{hf} ranges from 497.2 to 500.9 kOe. These parameters are consistent with high-spin Fe^{3+} in the orthoferrite phase. A similar room-temperature IS of 0.25 mm/s has been reported for $LaFeO_3$ exhibiting a single magnetic sextet, supporting the Fe^{3+} assignment[13]. The octahedral coordination of Fe is consistent with the orthorhombic structural model identified by XRD. The fitted QS values are zero for all compositions at the reported precision. Together, these results suggest broadly comparable local Fe hyperfine environments across the investigated compositions despite the composition-dependent structural changes. However, the similarity of these parameters does not establish identical Fe-O bond geometries.

The Mössbauer results provide a local perspective on the compositional differences observed by VSM. Despite their contrasting high-field magnetization, coercivity, and remanence, $YFeO_3$ and the magnetic rare-earth orthoferrites exhibit similar Fe hyperfine fields and the same reported IS values. The differences in the bulk magnetic response are therefore not accompanied by a resolved change in the predominant Fe valence state or a large variation in H_{hf}. This comparison is consistent with an additional rare-earth contribution to the high-field magnetization, as discussed in the preceding section, but does not independently quantify that contribution. Overall, the R-site composition modifies the lattice and macroscopic magnetic response while preserving a broadly similar local Fe^{3+} hyperfine environment at room temperature.

Dielectric Properties

Figure 5(a) and (b) show the room-temperature frequency dependence of the dielectric constant (ε′) and dielectric loss tangent (tan δ), respectively, for $RFeO_3$ (R = Y, Tb, Dy, Ho, and Er) over the frequency range of 10 Hz-1 MHz. All compositions exhibit an overall decrease in ε′ with increasing frequency, with the strongest dispersion observed for $YFeO_3$. At 10 Hz, $YFeO_3$ exhibits an ε′ of 6071.27, whereas the other compositions show values ranging from 222.72 to 347.20. This pronounced low-frequency contrast diminishes as the frequency increases. At 1 MHz, all five compositions exhibit ε′ values within a much narrower range of 7.26-7.86.

The enhanced low-frequency permittivity and its decrease with increasing frequency are compatible with slow interfacial polarization processes. In electrically heterogeneous ceramics, charge accumulation at interfaces between regions of different conductivity can enhance the apparent permittivity at low frequencies[14]. As the frequency increases, these contributions become less effective, resulting in dielectric dispersion. Maxwell-Wagner-type polarization has also been discussed for $DyFeO_3$ at elevated temperatures in conjunction with impedance analysis of grain and grain-boundary responses[14]. This provides a possible interpretation of the present frequency dependence. However, the dielectric curves alone do not distinguish contributions from internal interfaces and sample-electrode interfaces, and the large low-frequency ε′ of $YFeO_3$ cannot be assigned solely to intrinsic lattice polarization.

The loss-tangent spectra show a distinct compositional dependence. $YFeO_3$ exhibits a broad maximum, with the largest measured tan δ of 25.97 at 197.35 Hz, followed by a substantial decrease with increasing frequency. In contrast, the other four compositions show an overall decrease in tan δ across most of the measured range without a comparable low-frequency maximum. At 10 Hz, $HoFeO_3$ exhibits the lowest tan δ of 3.41, whereas the values for $TbFeO_3$, $DyFeO_3$, and $ErFeO_3$ range from 9.98 to 20.36. At the high-frequency end, all compositions exhibit a slight upturn in tan δ after reaching their respective minima. The broad maximum in $YFeO_3$ suggests a relaxation-related response, although its microscopic origin cannot be established from the present spectra alone.

Overall, the dielectric contrast among the compositions is most pronounced at low frequencies. $YFeO_3$ exhibits a large low-frequency permittivity together with substantial dielectric loss, whereas the permittivity values fall within a narrow range of 7.26-7.86 at 1 MHz. The enhanced permittivity of $YFeO_3$ is therefore strongly frequency dependent and is not accompanied by a uniformly low-loss response. The combined permittivity and loss spectra are consistent with a contribution from slow interfacial polarization to the low-frequency dielectric response.

Conclusions

Single-phase orthorhombic $RFeO_3$ (R = Y, Tb, Dy, Ho, and Er) powders were synthesized by a sol-gel auto-combustion method and investigated using complementary structural, magnetic, dielectric, and Mössbauer measurements. X-ray diffraction revealed a systematic decrease in unit-cell volume with decreasing R^{3+} ionic radius, while Raman spectra showed composition-dependent band shifts within the lanthanide series. The orthoferrites containing magnetic rare-earth ions exhibited larger magnetization at 20 kOe but lower coercivity and remanence than $YFeO_3$, demonstrating distinct compositional trends in high-field magnetization and hysteresis. In contrast, all room-temperature Mössbauer spectra were described by a single magnetic sextet, with isomer shifts of 0.24 mm/s and hyperfine fields of 497.2-500.9 kOe, consistent with high-spin Fe^{3+} and broadly similar local Fe hyperfine environments. Dielectric measurements revealed strong frequency dispersion, with the enhanced low-frequency permittivity of $YFeO_3$ accompanied by substantial dielectric loss and a broad loss-tangent maximum near 200 Hz. The differences in permittivity among the compositions became much smaller at 1 MHz. Overall, the results show that composition-dependent lattice and macroscopic property variations coexist with a largely retained local Fe^{3+} hyperfine environment, highlighting the importance of considering both structural changes and the magnetic character of the R-site ion when interpreting the magnetic response.

Acknowledgments

This research was supported by the ANCHOR program through the Daejeon ANCHOR Center, funded by the Ministry of Education(MOE) and the Daejeon Metropolitan City, Republic of Korea.(2026-ANCHOR-06-001)

References

1. Cao S et al (2016) Tuning the weak ferromagnetic states in dysprosium orthoferrite. Sci Rep **6**:37529
2. Weber MC, Guennou M, Zhao HJ, Íñiguez J, Vilarinho R, Almeida A, Moreira JA, Kreisel J (2016) Raman spectroscopy of rare-earth orthoferrites $RFeO_3$ (R = La, Sm, Eu, Gd, Tb, Dy). Phys Rev B **94**:214103
3. White RL (1969) Review of recent work on the magnetic and spectroscopic properties of the rare-earth orthoferrites. J Appl Phys **40**:1061–1069
4. Das S, Ross A, Ma XX, Becker S, Schmitt C, van Duijn F, Galindez-Ruales EF, Fuhrmann F, Syskaki M-A, Ebels U, Baltz V, Barra A-L, Chen HY, Jakob G, Cao SX, Sinova J, Gomonay O, Lebrun R, Kläui M (2022) Anisotropic long-range spin transport in canted antiferromagnetic orthoferrite $YFeO_3$. Nat Commun **13**:6140
5. Nakhaei M, Khoshnoud DS (2021) Structural, magnetic, and electrical properties of $RFeO_3$ (R = Dy, Ho, Yb & Lu) compounds. J Mater Sci Mater Electron **32**:14286–14300
6. Moskvin A (2021) Structure–property relationships for weak ferromagnetic perovskites. Magnetochemistry **7**:111
7. Nakhaei M, Khoshnoud DS (2021) Study on structural, magnetic and electrical properties of $ReFeO_3$ (Re = La, Pr, Nd, Sm & Gd) orthoferrites. Physica B **612**:412899
8. Wang Z-Q, Mu Y, Zeng Z-Y, Chen X-R, Chen Q-F (2019) First-principles study of elastic, dielectric, and vibrational properties of orthoferrites $RFeO_3$ (R = Ho, Er, Tm and Lu). Mater Res Express **6**:055605
9. Seo JY, Choi H, Kim CS, Uhm YR, Sun GM (2020) Determination of the magnetic structure and properties of the FeS compound by using Mössbauer spectroscopy. J Korean Phys Soc **77**:898–902
10. Kim W, Moon SJ, Kim CS (2008) Mössbauer studies of Fe^{2+} and Fe^{3+} mixed state in ilmenite–hematite solid solution. Hyperfine Interact **185**:167–171

11. Vilarinho R, Bouvier P, Guennou M, Peral I, Weber MC, Tavares P, Mihalik M Jr, Mihalik M, Garbarino G, Mezouar M, Kreisel J, Almeida A, Moreira JA (2019) Crossover in the pressure evolution of elementary distortions in $RFeO_3$ perovskites and its impact on their phase transition. Phys Rev B **99**:064109
12. Belov KP, Kadomtseva AM, Levitin RZ (1965) The magnetic susceptibility of rare-earth orthoferrites in strong magnetic fields. Sov Phys JETP **20**:291–293
13. Manchón-Gordón AF, Sánchez-Jiménez PE, Blázquez JS, Perejón A, Pérez-Maqueda LA (2023) Structural, vibrational, and magnetic characterization of orthoferrite $LaFeO_3$ ceramic prepared by reaction flash sintering. Materials **16**:1019
14. Yadav A, Sahoo S, Chin WK, Panda D, Adegbite PI, Tamang B, Mahbub R, Lai RY, Shield JE, Choudhary RNP, Rangari V (2025) Synthesis, structural, dielectric, electrical, and magnetic characterization of dysprosium orthoferrite nanoparticles. ACS Omega **10**:36931–36945

372 **Table 1** Refined structural parameters of $RFeO_3$ (R = Y, Tb, Dy, Ho, Er)

Material	Structure (Space group)	R^{3+} ionic radii (pm)	Tolerance factor	Lattice constant (Å)			Cell volume ($Å^3$)
				a	b	c	
EFO	Orthorhombic (*Pbnm*)	100.4	0.8312	5.2629	5.5811	7.5951	223.0891
HFO		101.5	0.8350	5.2813	5.5881	7.6084	224.5424
YFO		101.9	0.8364	5.2822	5.5928	7.6066	224.7164
DFO		102.7	0.8391	5.3041	5.5938	7.6248	226.2284
TFO		104	0.8436	5.3283	5.5983	7.6430	227.9863

373

374

375 **Table 2** Raman band positions of $RFeO_3$ (R = Tb, Dy, Ho, Er) at 295 K

Sample	Peak position (cm^{-1})						
	P1	P2	P3	P4	P5	P6	P7
EFO	105.385	133.423	152.142	262.940	326.406	412.182	486.716
HFO	105.004	133.095	151.360	257.169	322.162	406.815	480.178
DFO	105.481	133.410	150.119	254.569	317.597	400.510	475.538
TFO	105.644	133.325	149.353	246.637	310.534	393.173	467.006

376

377

Table 3 Room-temperature magnetic parameters of $RFeO_3$ (R = Y, Tb, Dy, Ho, Er)

Material	Net magnetization at 20 kOe (M_{net})(emu/g)	Coercivity (H_c)(Oe)	Remanent magnetization (M_r)(emu/g)
EFO	2.9633	388.17	0.0673
HFO	3.5535	406.19	0.0844
YFO	0.6759	10,294	0.4888
DFO	3.5110	374.09	0.0864
TFO	3.2982	179.63	0.0325

381 **Table 4** Room-temperature Mössbauer hyperfine parameters of $RFeO_3$ (R = Y, Tb, Dy, Ho,
382 Er)

	EFO	HFO	YFO	DFO	TFO
H_{hf} (kOe)	497.2	499.8	500.9	497.3	498.7
QS (mm/s)	0	0	0	0	0
δ (mm/s)	0.24	0.24	0.24	0.24	0.24
Area (%)			100		
Ionic state			Fe^{3+} ($3d^5$) High spin		

383

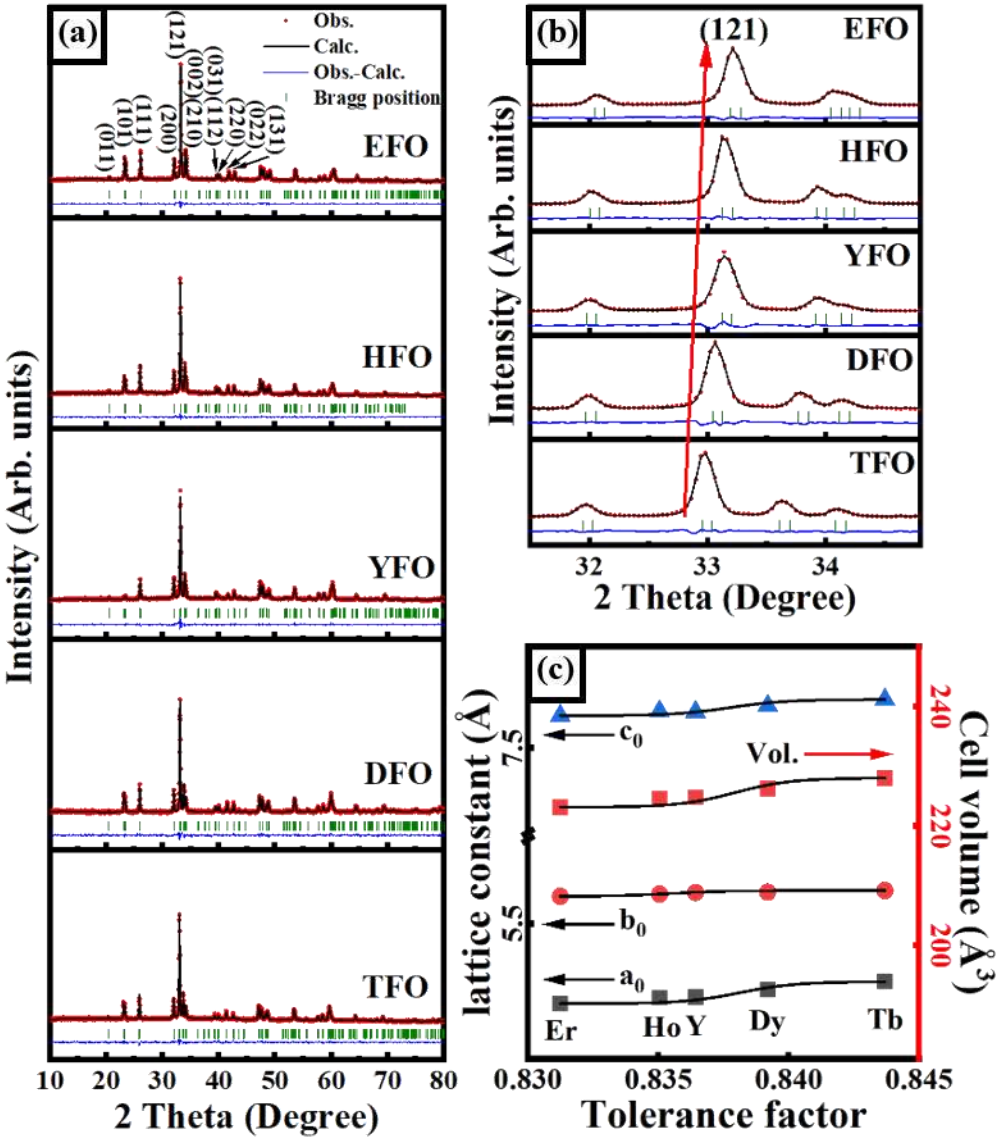
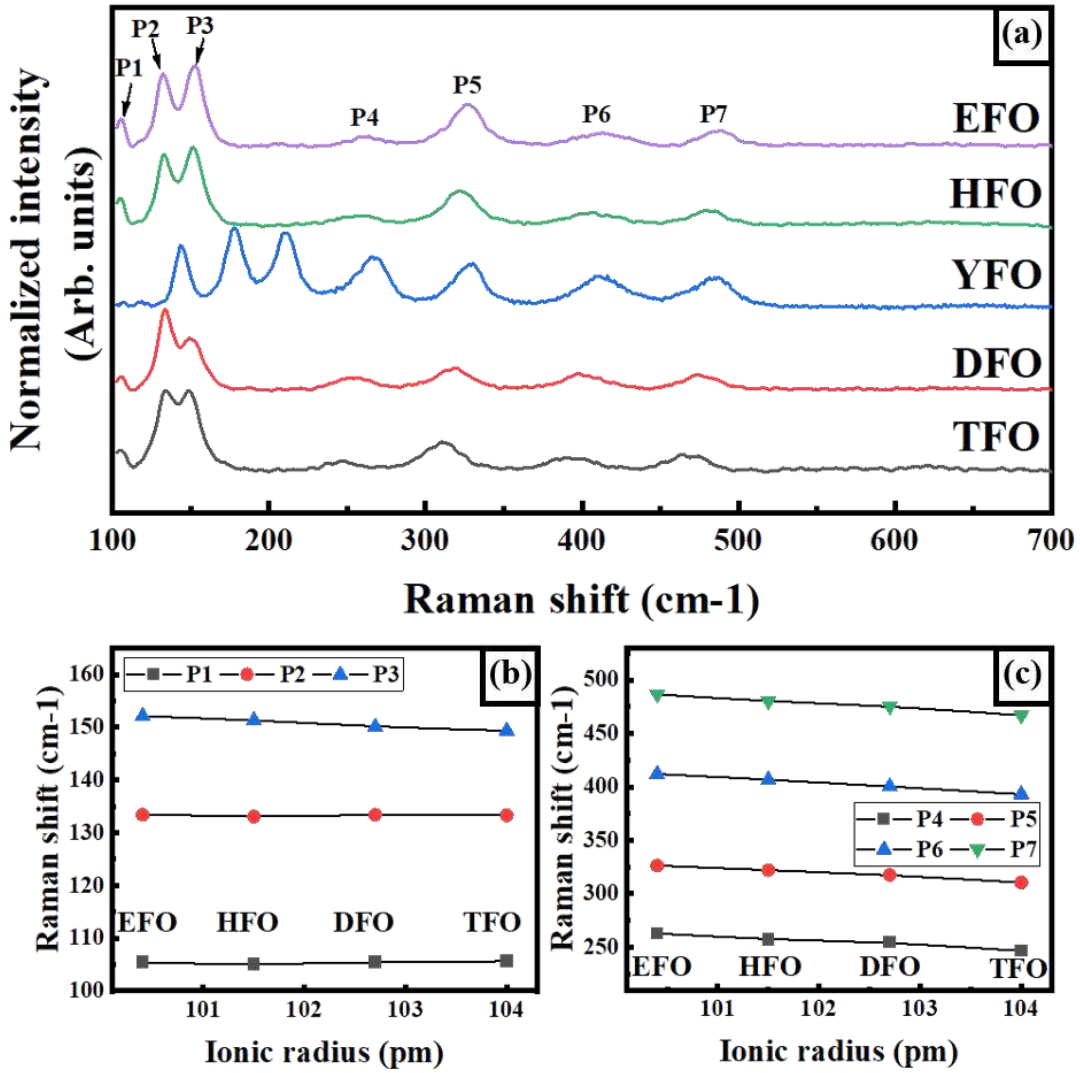


Fig. 1 (a) X-ray diffraction patterns and Rietveld refinement profiles of $RFeO_3$ (R = Y, Tb, Dy, Ho, and Er). (b) Enlarged diffraction patterns near $2\theta = 33°$. (c) Lattice parameters and unit-cell volumes as a function of the tolerance factor.

389



390
391 **Fig. 2** (a) Raman spectra of $RFeO_3$ (R = Y, Tb, Dy, Ho, and Er).
392 Fitted positions of (b) P1-P3 and (c) P4-P7 as a function of R^{3+} ionic radius for R = Tb,
393 Dy, Ho, and Er. P1-P7 identify the bands compared across the lanthanide compositions.
394

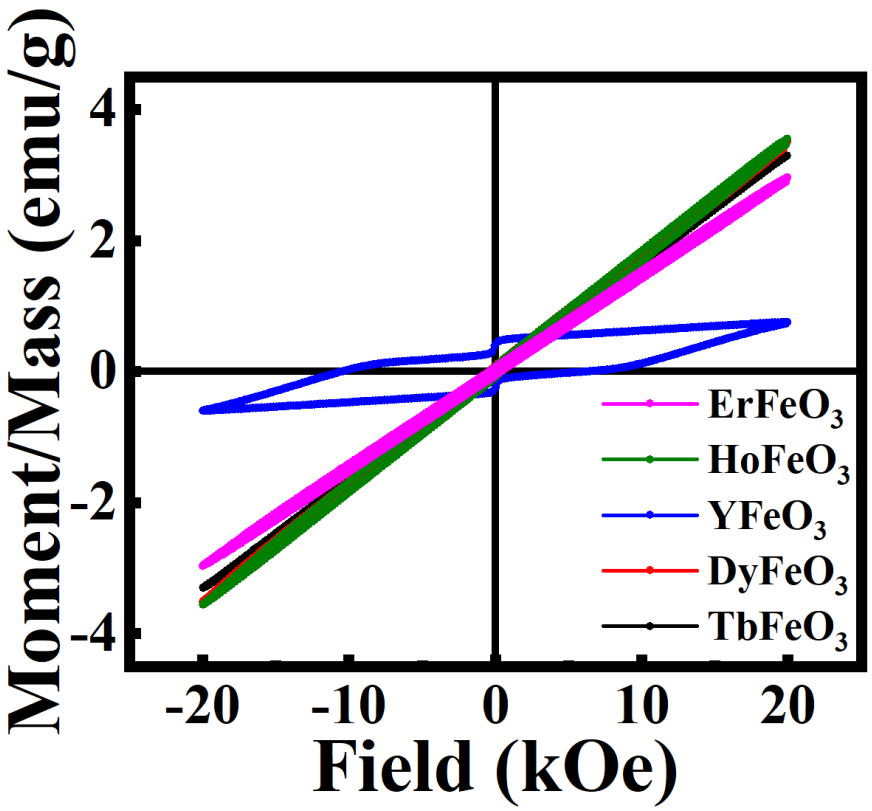
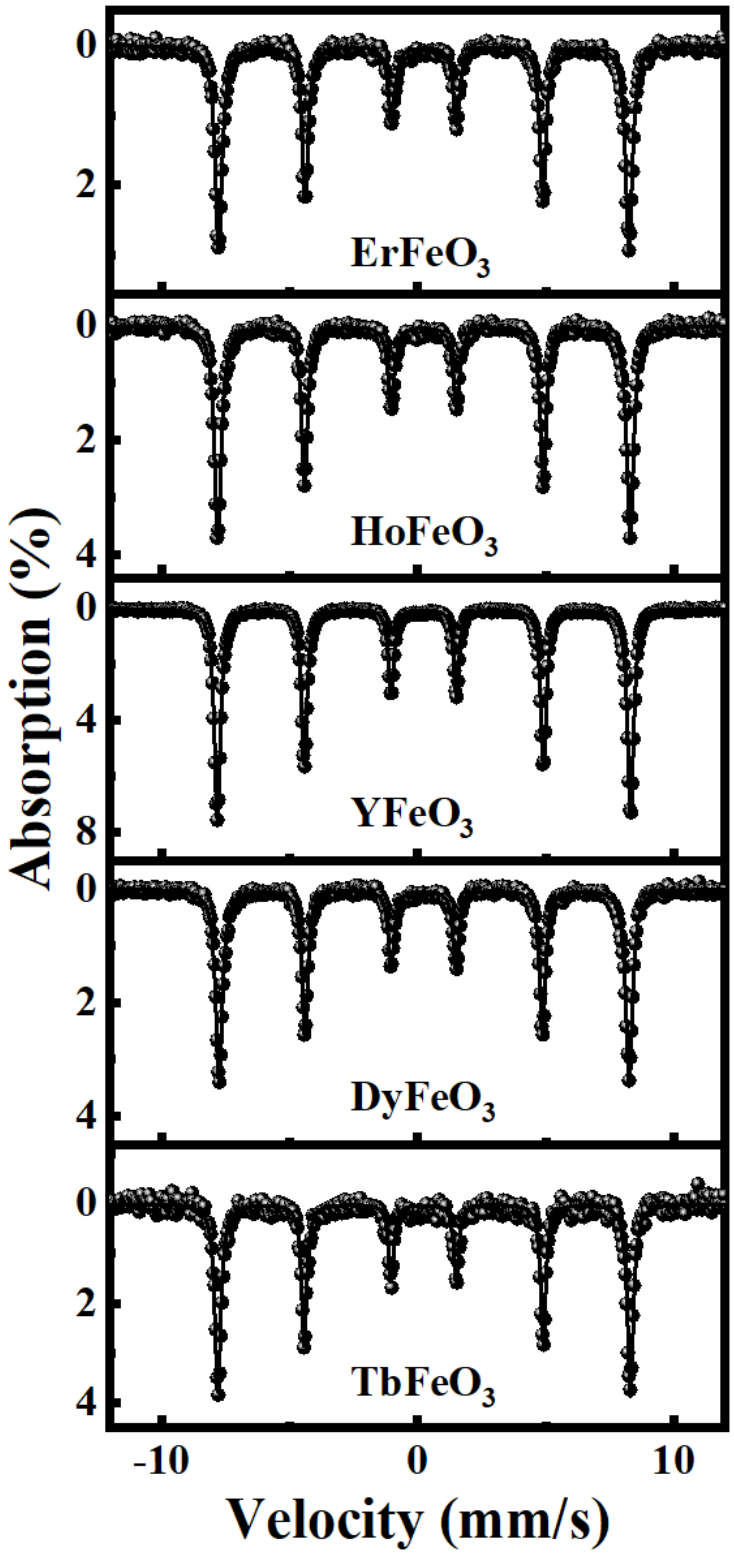


Fig. 3 Room-temperature magnetization–field (M–H) curves of $RFeO_3$ (R = Y, Tb, Dy, Ho, and Er) powders measured over an applied field range of −20 to +20 kOe.



399
400 **Fig. 4** Room-temperature ^{57}Fe Mössbauer spectra of $RFeO_3$ (R = Y, Tb, Dy, Ho, and Er).

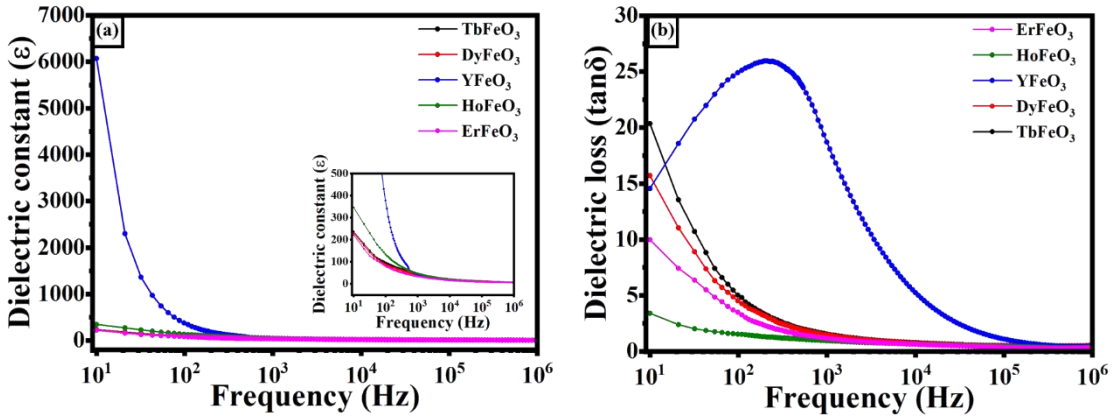


Fig. 5 Room-temperature frequency dependence of (a) the dielectric constant (ε') and (b) the dielectric loss tangent (tan δ) of $RFeO_3$ (R = Y, Tb, Dy, Ho, and Er) over 10 Hz–1 MHz. The inset in (a) shows an enlarged view of the lower-permittivity region.